Plasma Chem Plasma Process
DOI 10.1007/s11090-017-9859-x

ORIGINAL PAPER

Modelling of the Plasma–Sheath Boundary Region in Wall-Stabilized Arc Plasmas: Unipolar Discharge Properties

B. Mancinelli[1] · L. Prevosto[2] · J. C. Chamorro[1] · F. O. Minotti[3,4] · H. Kelly[1]

Received: 28 June 2017 / Accepted: 28 October 2017

Abstract A two-dimensional model of the non-equilibrium unipolar discharge occurring in the plasma–sheath boundary region of a transferred-arc was developed. This model was used to study the current transfer to the nozzle (1 mm diameter) of a 30 A arc cutting torch operated with oxygen. The energy balance and chemistry processes in the discharge were described by using a kinetic block of 45 elementary reactions and processes with the participation of 13 species including electronically excited particles. The nonlocal transport of electrons was accounted for into the fluid model. The dependence of the ion mobility with the electric field was also considered. Basic discharge properties were described. It has been found that a large part ($\sim$ 80%) of the total electric power (1700 mW) delivered in the bulk of the sheath region is spent in heating the positive ions and further dissipated through collisions with the neutral particles. The results also showed that the electron energy loss in inelastic collisions represents only $\sim$ 25% of the electron power and that about 63% of the power spent on gas heating is produced by the ion–molecule reaction, the electron–ion and ion–ion recombination reactions, and by the electron attachment. The rest of the power converted into heat is contributed by dissociation by electron-impact, dissociative ionization and quenching of $O(^1D)$. Some fast gas heating channels which are expected to play a key role in the double-arcing phenomena in oxygen gas were also identified.

✉ L. Prevosto
prevosto@waycom.com.ar

[1] Grupo de Descargas Eléctricas, Departamento Ing. Electromecánica, Facultad Regional Venado Tuerto, UTN, Laprida 651, Venado Tuerto, Santa Fe, Argentina

[2] Grupo de Descargas Eléctricas, Departamento Ing. Electromecánica, Facultad Regional Venado Tuerto, Universidad Tecnológica Nacional, CONICET, Laprida 651, Venado Tuerto, Santa Fe, Argentina

[3] Departamento de Física, Facultad de Ciencias Exactas y Naturales, Universidad de Buenos Aires, Buenos Aires, Argentina

[4] CONICET- Universidad de Buenos Aires, Instituto de Física del Plasma (INFIP), Buenos Aires, Argentina

Published online: 02 November 2017

Keywords Plasma–sheath · Wall-stabilized arc · Unipolar discharge

Introduction

The problem of sheath formation at the plasma boundary is of particular importance for nearly all technological applications where the plasma is confined (totally or partially) to a finite volume by solid walls [1–7], as in wall-stabilized arcs [8–11]. In the case of plasma arc cutting [e.g., 10], the case this paper is dedicated to, the wall is a nozzle with an inner diameter of 1–3 mm and a length of 5–10 mm, where the gas is tangentially injected at a pressure of few atmospheres. The arc current is in the order of 10–1000 A. The intense convective cooling at the arc fringes due to the vortex flow enhances the power dissipation per unit length of the arc column, which in turn results in high axial electric field values. Typically, arc voltage drops inside the nozzle of about 50 V or even higher are usually reached [12, 13].

During the cutting arc process the nozzle behaves as a floating conductor (i.e., it is not electrically connected to any part of the torch circuit). However, since the metallic nozzle itself is at a constant floating voltage facing a plasma with a large axial voltage variation, the zero-current balance cannot be fulfilled locally (i.e., by an ambipolar flux to the nozzle), but globally (along the whole collecting area of the nozzle): electrons flow to that part of the nozzle which is close to the cathode whereas that part of the nozzle which is close to the anode receives the ion current. The electrical connection of these currents is through the metallic nozzle [10]. This means that a minor fraction of the arc current recirculates through the nozzle, thus indicating the existence of some kind of high-pressure, non-equilibrium discharge in the plasma–sheath boundary region adjacent to the nozzle wall. In this kind of discharge one electrode (the nozzle) serves both as cathode and anode, in contrast to usual discharges, a feature resembling unipolar discharges [14, 15]. A sketch of this unipolar discharge in the plasma–sheath boundary region of a cutting arc torch is presented in Fig. 1. The arrow in the current loop through the nozzle body indicates its conventional direction. We note that the conditions studied in this work are those corresponding to the normal operation of the torch, with most of the current circulating in the plasma core. The small loop current ($\sim$ 0.05 A for a main arc current of 30 A, according to what is inferred from Fig. 6a in the "Numerical Results" section) is a feature of this mode of operation, due to the nozzle being in contact with regions of plasma with differing characteristics. The current loop has axial symmetry, that is, it takes place all around the nozzle, and no double-arcing is involved.

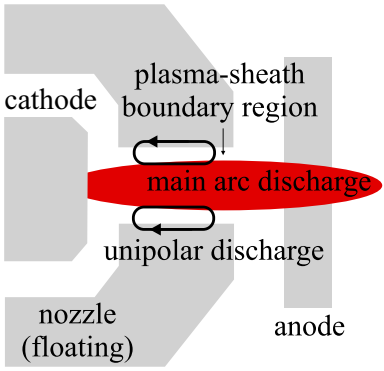

Fig. 1 Sketch of the unipolar discharge in the plasma–sheath boundary region of a transferred arc plasma torch

With increased applied fields (as for instance, for a too large arc current [10]), various secondary processes come into operation in the plasma–sheath boundary region, and ultimately a constricted-type discharge carrying a substantial part of the arc current will flow through the floating nozzle, likely destroying it. Such type of arc instability is called 'double-arcing' [10]. Relatively little [12, 13, 16, 17] has been done to explore and understand the double-arcing phenomenon, especially considering that it is one of the main drawbacks that limit the capabilities of the plasma arc cutting process. The properties of the non-equilibrium discharge in the plasma–sheath boundary region previous to the double-arcing phenomenon are even less known [17–19]. However, a good understanding of the features of such non-equilibrium discharge is necessary both from the point of view of the basic physics of cutting arcs, and also for a further study of the double-arcing phenomena.

A two-dimensional (2D) fluid modeling of the plasma–sheath boundary layer in a cutting arc torch was presented in [18]. The ion transport was described by a continuity equation under the drift-diffusion approximation with the source term taken as zero. The basic assumption was that no significant ionization occurred in the sheath because both the electron density and the thickness of the sheath were small. A 2D fluid modelling with a reduced kinetic scheme (including ionization of heavy particles by electron impact, electron attachment, electron detachment, electron–ion recombination and ion–ion recombination) was presented in [17]. The gas temperature was assumed to be constant (1000 K). The 'local field approximation' (i.e., the electron energy gain due to the field at a given location and time is exactly balanced by the collisional losses at the same location and time) was used for the calculation of the transport and rate coefficients of the electrons.

In this work, an improved numerical investigation of the properties of the non-equilibrium unipolar discharge in the plasma–sheath boundary region of a cutting arc torch operated with oxygen is presented. This work is based on a previously reported fluid model [17]. In order to overcome the disadvantages associated with the local field approximation, and incorporate the nonlocal transport of electrons into the fluid model, the calculations of the electron transport (mobility and diffusion) coefficients as well as the kinetic coefficients (electron-impact reaction rates for excitation, dissociation and ionization processes), were performed by solving the kinetic Boltzmann equation as functions of the electron temperature rather than as functions of the local value of the electric field (e.g., [20]). In addition, the dependence of the ion mobility with the electric field was considered. The spatial distribution of the electron temperature within this model was obtained from the solution of the energy balance equation for electrons, which along with the volume processes takes also account of the energy transfer by heat conduction. Moreover, for this investigation the number of species and reactions was increased significantly, including several processes with the participation of electronically excited particles describing the gas energy balance and charged particles kinetic processes for a pure oxygen discharge.

The obtained unipolar discharge properties will be used to investigate the double-arcing phenomena with the focus on the gas heating processes, and will be presented in a future paper.

Fluid Model

Model Domain

At high gas pressure, when both the plasma and the sheath are collisional, plasma and sheath join smoothly, without the need of a transitional layer [3, 5]. Thus, the sheath edge

coincides with the unperturbed (quasi-neutral) non-local thermal equilibrium (non-LTE) arc plasma. The model geometry of the plasma–sheath boundary region (4.5 mm in length and 8.4 μm in thickness [17]) contiguous to the floating nozzle (bore radius of 0.5 mm, 4.5 mm in length) of a low-current (30 A) oxygen-operated arc cutting torch, is given in Fig. 2. The detailed geometry of the torch used can be found elsewhere [17]. Since the layer remains thin as compared with the nozzle orifice radius, a planar geometry was used (x and y being the axial and normal to the nozzle wall coordinates, respectively).

The thickness of the model geometry corresponded to an estimation of the initial radial extent of the space-charge sheath which separates the non-LTE plasma to the nozzle wall. For a plasma density at the arc boundary being an almost linearly decreasing function of the axial position, varying from 1.5×10^{18} m^{-3} at the nozzle inlet, to 1.4×10^{20} m^{-3} at the nozzle exit, and the electron temperature about 0.5 eV [17]; the sheath thickness, found by invoking the collisional sheath model [21], resulted of the order of few Debye lengths ($\sim$ 0.4–4 $\times$ 10^{-6} m) depending on the local values of the plasma density and plasma–nozzle voltage drop. According to previously published results (Fig. 2, [21]) the sheath extension can reach only two Debye lengths for a sufficiently highly collisional sheath with a low voltage drop across it. Thus, for the extreme case in which the initial value of the sheath thickness at the nozzle inlet corresponds to a voltage drop of only 1 V (the arc voltage at the nozzle inlet was assumed as $-$ 80 V and at the initial time step the nozzle voltage was set to $-$ 81 V), the resulting sheath extension there was $\sim$ 2 Debye lengths since the electron temperature at the plasma side was about 0.5 eV. Hence, a quasi-neutral plasma can be safely assumed along of the whole nozzle at a boundary located at 8.4 μm from the nozzle wall for the highly collisional sheath considered.

Equations

All the plasma species (including electrons) were treated within the fluid-like approximation [17, 18]. The model includes time-dependent continuity equations for the charged, ground-state atoms, and excited particles,

$$\frac{\partial}{\partial t}(n_k) + \nabla \cdot \bar{\Gamma}_k = S_k, \tag{1}$$

where the particle flux is expressed in the drift-diffusion approximation,

$$\bar{\Gamma}_k = \mathrm{sgn}(q_k) n_k \mu_k \bar{E} - D_k \nabla n_k, \tag{2}$$

(see e.g., [22]). The density of the dominant species (i.e., the ground-state molecules) was obtained from the constancy of the total pressure.

The electric field was obtained from the solution of the Poisson's equation in the electrostatic approximation,

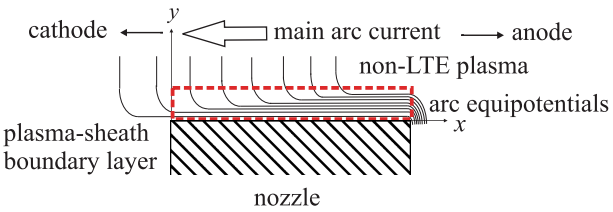

Fig. 2 Sketch of the plasma–sheath boundary region

$$\varepsilon_0 \nabla \cdot \bar{E} \sum_k q_k n_k, \quad \bar{E} = -\nabla \phi. \tag{3}$$

In these equations, subscript k indicates the kth species. $\bar{E}$ and ϕ are the electric field and the electrostatic potential, q is the charge, ε_0 is the dielectric constant, μ and D are the particle mobility and diffusion coefficients, and S is the particle creation rate.

Equations (1)–(3), with particle transport coefficients and volume source terms in the particle balance equations specified, form the traditional 'simple fluid' model [23]. Within this model, mobility and diffusion coefficients as well as the particle creation rates, in general, are defined as functions of the reduced electric field E/n (i.e., under the 'local field approximation'). The Einstein relation between mobility and diffusion is assumed to be valid. Here, n denotes the gas density. In order to incorporate the nonlocal transport of electrons into the fluid model, the electron energy equation was included into the set of 'extended fluid model' equations (see, e.g., [20, 22–24]),

$$\frac{\partial}{\partial t}(n_\varepsilon) + \nabla \cdot \bar{\Gamma}_\varepsilon = -e\bar{E} \cdot \bar{\Gamma}_e - \sum_j \Delta E_j R_j, \tag{4}$$

where $n_\varepsilon = n_e \bar{\varepsilon}$ is the electron energy density, $\bar{\varepsilon}$ being the mean electron energy. In Eq. (4) the electron mean energy is assumed to result mainly from random motion, so that it is consistent to define the 'effective' electron temperature as $k_b T_e \equiv 2/3\bar{\varepsilon}$ (e.g., [20, 23–26]), k_b being the Boltzmann's constant. However, the Einstein relation was not used and the rate coefficients for almost all electron-impact processes were calculated without assuming the electron energy distribution function (EEDF) to be Maxwellian. Notice that the EEDF may differ substantially from the Maxwellian one for the conditions considered due to the rather low-electron density. In this model, a more accurate approach to the determination of the rate coefficients for such electron processes (excitation, dissociation, ionization) was used, based on finding the EEDF by means of a solution of the electron Boltzmann equation [25]. e is the modulus of the electron charge; and the flux of the electron energy density is,

$$\bar{\Gamma}_\varepsilon = -n_e \mu_\varepsilon \bar{E} - D_\varepsilon \nabla n_e. \tag{5}$$

In the source term of Eq. (4), the first term describes the Joule heating (or cooling) of electrons in the electric field while the second term describes the energy exchanged in inelastic collisions. ΔE_j and R_j are the energy loss (or gain) due to inelastic collision and the corresponding reaction rate, respectively. The small term representing the electrons elastic loss was neglected in Eq. (4). According to a numerical solution of the Boltzmann equation for electrons [25], the fractional electron power transferred in elastic collisions in oxygen is 0.4% for $T_\mathrm{e} = 0.5$ eV and 0.05% for 5 eV.

The mean translational energy of the neutral heavy species (gas) was described by the equation,

$$\frac{\partial}{\partial t}\left(n c_p T_\mathrm{g}\right) + \nabla \cdot \left(-\kappa^* \nabla T_\mathrm{g}\right) = Q_\mathrm{R} + Q_{ion}, \quad c_p \equiv \frac{1}{n}\sum_k c_{p,k} n_k, \tag{6}$$

where $c_{\mathrm{p,k}}$ is the specific heat of the (neutral) species k (= 7/2 k_b for a diatomic molecule and 5/2 k_b for an atom), Q_R is the 'fast' gas heating rate term due to the electronic-to-translational relaxation energy (e.g., [26–30]), Q_ion is the gas heating rate term due to elastic collision with hot ions in the plasma–sheath boundary region, and κ^* is the gas

thermal conductivity. The material quantity κ^* was calculated by subtracting from the equilibrium κ value (taken form [11]), the contribution related to the chemical reactions (for oxygen and other gases at atmospheric pressure, the electron contribution is negligible small for temperatures < 7000 K under LTE conditions [11]). In equilibrium conditions at low temperatures (when the degree of ionization is low) the reactive contribution is mainly due to dissociation. The corrected value of the gas thermal conductivity was then obtained as,

$$\kappa^* = \kappa - \varepsilon_{diss} D_n \frac{p}{k_b T_g} \frac{\partial}{\partial T_g} \left(\frac{1 - \alpha_D}{1 + \alpha_D} \right), \tag{7}$$

where D_n and ε_{diss} (= 5.12 eV [28]) are the diffusion coefficient and the dissociation limit ($O(^3P) + O(^3P)$) of the oxygen molecule, and p and α_D are the pressure and the degree of dissociation of the gas (calculated from the dissociation constant [11] for an oxygen gas); respectively.

In the model considered, the contribution of the fast-vibrational relaxation of oxygen molecules into gas heating was neglected in Eq. (6). Consequently, in Eq. (4) it was assumed that the vibrational temperature of molecules was close to the gas temperature, so the electrons were not heated in superelastic collisions with vibrationally excited oxygen molecules. This is true when the energy deposited into vibrational degrees of freedom is sufficiently small. Note that in contrast with nitrogen discharges, large differences between vibrational and gas temperatures are difficult to achieve in oxygen discharges due to both high probabilities of vibrational–translational transitions in O_2(X, v)–O collisions and small rate coefficients for electron excitation of oxygen vibrational levels (v) [22]. Therefore, pure vibrational mechanisms are ineffective for gas heating in low-temperature pure oxygen discharges and were neglected in the present calculations. Moreover, the electron-impact rotational excitation of oxygen molecules (followed by the rapid rotational–translational relaxation) was also neglected.

Rate Coefficients

Calculations were performed for a pure oxygen gas, and thirteen plasma species were taken into account: electrons (e), singly charged positive ions (O^+), molecular ions (O_2^+), cluster ions (O_4^+), singly charged negative ions (O_2^-), oxygen molecular metastable ($O_2(a^1\Delta_g)$), the predissociation states $O_2(A^3\Sigma_u^+)$, $O_2(B^3\Sigma_u^-)$ and O_2^*, oxygen atomic metastable ($O(^1D)$) and ($O(^1S)$); ground-state molecules (O_2 ($X^3\Sigma_g^-$)) and atoms ($O(^3P)$). The model takes into consideration 45 elementary reactions and processes that influence gas heating, excitation and de-excitation of electronic states of oxygen, dissociation due to electron impact, generation and loss of the charged particles due to direct, stepwise and dissociative ionization, electron attachment/detachment, volume electron–ion and ion–ion recombination; diffusion and surface reactions. The set of reactions used is given in Table 1. It should be noted that the uncertainty in the rate constants used for the oxygen–electron chemistry varies between 5 and 30%, for the oxygen-neutral chemistry between 10 and 100%; and for the ion-chemistry of the oxygen between 10 and 300% (the later for the three-body ion–ion recombination reactions (R37) in Table 1) [42]. Thus, the uncertainty introduced into the model from the uncertainty in the rate constants is likely to be significant.

Although the formation of O_2^- due to three-body electron attachment to O_2 ($X^3\Sigma_g^-$) was accounted for in the model [26], previous measurements carried out using the nozzle itself as a peripheral Langmuir probe have shown that the electron attachment does not play a

Table 1 Elementary reactions and processes involved in the kinetic model

No.	Reaction	ΔE (eV)	k [m^3/s or m^6/s], D [m^2/s], γ_q	References
Electron-impact excitation and dissociation				
R1	$e + O_2(X^3\Sigma_g^-) \rightarrow e + O_2(a^1\Delta_g)$	0.98	$k_1 = f(T_e)$	Boltzmann Solver [25]
R2	$e + O(^3P) \rightarrow e + O(^1D)$	1.967	$k_2 = f(T_e)$	Boltzmann Solver [25]
R3	$e + O(^3P) \rightarrow e + O(^1S)$	4.189	$k_3 = f(T_e)$	Boltzmann Solver [25]
R4	$e + O_2(X^3\Sigma_g^-) \rightarrow e + O_2(A^3\Sigma_u^+)$ $O_2(A^3\Sigma_u^+) \rightarrow O(^3P) + O(^3P) + \varepsilon_4$	6.00	$k_4 = f(T_e)$	Boltzmann Solver [25]
R5	$e + O_2(X^3\Sigma_g^-) \rightarrow e + O_2(B^3\Sigma_u^-)$ $O_2(B^3\Sigma_u^-) \rightarrow O(^3P) + O(^1D) + \varepsilon_5$	8.40	$k_5 = f(T_e)$	Boltzmann Solver [25]
R6	$e + O_2(X^3\Sigma_g^-) \rightarrow e + O_2^*$ $O_2^* \rightarrow O(^3P) + O(^1S) + \varepsilon_6$	9.97	$k_6 = f(T_e)$	Boltzmann Solver [25]
Electron-impact ionization				
R7	$e + O_2(X^3\Sigma_g^-) \rightarrow e + e + O_2^+$	12.06	$k_7 = f(T_e)$	Boltzmann Solver [25]
R8	$e + O_2(a^1\Delta_g) \rightarrow e + e + O_2^+$	11.08	$k_8 = k_7 \times \exp(0.98/T_e)$	Boltzmann Solver [25]. Threshold reduced
R9	$e + O_2(X^3\Sigma_g^-) \rightarrow e + e + O^+ + O(^3P) + \varepsilon_9$	16.81	$k_9 = f(T_e)$	Calculated from cross-section data [31]
R10	$e + O_2(a^1\Delta_g) \rightarrow e + e + O^+ + O(^3P) + \varepsilon_{10}$	15.83	$k_{10} = k_9 \times \exp(0.98/T_e)$	Calculated from cross-section data [31]. Threshold reduced
R11	$e + O(^3P) \rightarrow e + e + O^+$	13.61	$k_{11} = f(T_e)$	Boltzmann Solver [25]
R12	$e + O(^1D) \rightarrow e + e + O^+$	11.64	$k_{12} = k_{11} \times \exp(1.967/T_e)$	Boltzmann Solver [25]. Threshold reduced
R13	$e + O(^1S) \rightarrow e + e + O^+$	9.42	$k_{13} = k_{11} \times \exp(4.189/T_e)$	Boltzmann Solver [25]. Threshold reduced
Quenching of excited particles				
R14	$O_2(a^1\Delta_g) + O_2(X^3\Sigma_g^-) \rightarrow O_2(X^3\Sigma_g^-) + O_2(X^3\Sigma_g^-,v) + \varepsilon_{14}$	0.0	$k_{14} = 2.2 \times 10^{-24} \times (T_g/300)^{0.8}$	[32]
R15	$O_2(a^1\Delta_g) + O(^3P) \rightarrow O_2(X^3\Sigma_g^-,v) + O(^3P) + \varepsilon_{15}$	0.0	$k_{15} = 7.0 \times 10^{-22}$	[32]
R16	$O(^1D) + O_2(X^3\Sigma_g^-) \rightarrow O(^3P) + O_2(X^3\Sigma_g^-,v) + \varepsilon_{16}$	0.0	$k_{16} = 6.4 \times 10^{-18} \times \exp(67/T_g)$	[32]

Table 1 continued

No.	Reaction	ΔE (eV)	k [m^3/s or m^6/s], D [m^2/s], γ_q	References
R17	$O(^1S) + O_2(X^3\Sigma_g^-) \rightarrow O(^1D) + O_2(X^3\Sigma_g^-,v) + \varepsilon_{17}$	0.0	$k_{17} = 0.31 \times 4.3 \times 10^{-18} \times \exp(-850/T_g)$	[32, 33]
R18	$O(^1S) + O_2(X^3\Sigma_g^-) \rightarrow O(^3P) + O_2(A,c,C)$	0.0	$k_{18} = 0.69 \times 4.3 \times 10^{-18} \times \exp(-850/T_g)$	[32, 33]
R19	$O(^1S) + O(^3P) \rightarrow O(^1D) + O(^3P) + \varepsilon_{19}$	0.0	$k_{19} = 5.0 \times 10^{-17} \times \exp(-301/T_g)$	[32]
R20	$O_2(a^1\Delta_g) + \text{wall} \rightarrow O_2(X^3\Sigma_g^-)$	0.0	$\gamma_{q20} \sim 8.5 \times 10^{-4}$	[34]
R21	$O(^1D) + \text{wall} \rightarrow O(^3P)$	0.0	$\gamma_{q21} \sim 1$	[34]
R22	$O(^1S) + \text{wall} \rightarrow O(^3P)$	0.0	$\gamma_{q22} \sim 1$	[34]
Ion-conversion				
R23	$O_4^+ + O_2(a^1\Delta_g) \rightarrow O_2^+ + O_2(X^3\Sigma_g^-) + O_2(X^3\Sigma_g^-) + \varepsilon_{23}$	0.0	$k_{23} = 1.0 \times 10^{-16}$	[32]
R24	$O_2^+ + O_2(X^3\Sigma_g^-) + O_2(X^3\Sigma_g^-) \rightarrow O_4^+ + O_2(X^3\Sigma_g^-) + \varepsilon_{24}$	0.0	$k_{24} = 2.4 \times 10^{-42} \times (300/T_{eff})^{3.2}$	[32]
R25	$O^+ + O_2(X^3\Sigma_g^-) \rightarrow O_2^+ + O(^3P) + \varepsilon_{25}$	0.0	$k_{25} = 3.3 \times 10^{-17} \times \exp(-0.00169 T_{eff})$	[32]
Electron–ion and ion–ion recombination				
R26	$e + O_2^+ \rightarrow O(^3P) + O(^3P) + \varepsilon_{26}$	0.0	$k_{26} = 0.32 \times 1.95 \times 10^{-13} \times (0.0258/T_e)^{0.7}$	[35]
R27	$e + O_2^+ \rightarrow O(^3P) + O(^1D) + \varepsilon_{27}$	0.0	$k_{27} = 0.43 \times 1.95 \times 10^{-13} \times (0.0258/T_e)^{0.7}$	[35]
R28	$e + O_2^+ \rightarrow O(^1D) + O(^1D) + \varepsilon_{28}$	0.0	$k_{28} = 0.20 \times 1.95 \times 10^{-13} \times (0.0258/T_e)^{0.7}$	[35]
R29	$e + O_2^+ \rightarrow O(^1D) + O(^1S) + \varepsilon_{29}$	0.0	$k_{29} = 0.05 \times 1.95 \times 10^{-13} \times (0.0258/T_e)^{0.7}$	[35]
R30	$e + e + O_2^+ \rightarrow e + O_2(X^3\Sigma_g^-)$	− 12.1	$k_{30} = 1.0 \times 10^{-30} \times (0.0258/T_e)^2$	[36]
R31	$e + O_4^+ \rightarrow O_2(X^3\Sigma_g^-) + O(^3P) + O(^3P) + \varepsilon_{31}$	0.42	$k_{31} = 0.32 \times P \times 42 \times 10^{-13} \times (0.0258/T_e)^{0.48}$ (*)	[37]
R32	$e + O_4^+ \rightarrow O_2(X^3\Sigma_g^-) + O(^3P) + O(^1D) + \varepsilon_{32}$	0.42	$k_{32} = 0.43 \times P \times 42 \times 10^{-13} \times (0.0258/T_e)^{0.48}$ (*)	[37]
R33	$e + O_4^+ \rightarrow O_2(X^3\Sigma_g^-) + O(^1D) + O(^1D) + \varepsilon_{33}$	0.42	$k_{33} = 0.20 \times P \times 42 \times 10^{-13} \times (0.0258/T_e)^{0.48}$ (*)	[37]

Table 1 continued

No.	Reaction	ΔE (eV)	k [m^3/s or m^6/s], D [m^2/s], γ_q	References
R34	$e + O_4^+ \rightarrow O_2(X^3\Sigma_g^-) + O(^1D) + O(^1S) + \varepsilon_{34}$	0.42	$k_{34} = 0.05 \times P \times 42 \times 10^{-13} \times (0.0258/T_e)^{0.48}$ (*)	[37]
R35	$e + O_4^+ \rightarrow O_2(X^3\Sigma_g^-) + O_2(X^3\Sigma_g^-) + \varepsilon_{35}$	0.42	$k_{35} = (1 - P) \times 42 \times 10^{-13} \times (0.0258/T_e)^{0.48}$ (*)	[32]
R36	$e + O^+ + O_2(X^3\Sigma_g^-) \rightarrow O(^3P) + O_2(X^3\Sigma_g^-) + \varepsilon_{36}$	0.0	$k_{36} = 6.0 \times 10^{-39} \times (0.0258/T_e)^{1.5}$	[32]
R37	$O_2^- + O_2^+ + O_2(X^3\Sigma_g^-) \rightarrow O_2(X^3\Sigma_g^-) + O_2(X^3\Sigma_g^-) + O_2(X^3\Sigma_g^-) + \varepsilon_{37}$	0.0	$k_{37} \sim 2 \times 10^{-37} \times (300/T_i)^{2.5}$	[32]
R38	$O_4^+ + O_2^- \rightarrow O_2(X^3\Sigma_g^-) + O_2(X^3\Sigma_g^-) + O_2(X^3\Sigma_g^-) + \varepsilon_{38}$	0.0	$k_{38} = 1 \times 10^{-13}$	[32]
Electron attachment and detachment				
R39	$e + O_2(X^3\Sigma_g^-) + O_2(X^3\Sigma_g^-) \rightarrow O_2^- + O_2(X^3\Sigma_g^-) + \varepsilon_{39}$	0.0	$k_{39} = 1.4 \times 10^{-41} \times (0.0258/T_e) \times \exp(-600/T_g) \times \exp(700/T_g - 0.0602/T_e)$	[32]
R40	$O_2^- + O_2(X^3\Sigma_g^-) \rightarrow O_2(X^3\Sigma_g^-) + O_2(X^3\Sigma_g^-) + e$	0.0	$k_{40} = 2.7 \times 10^{-16} \times (300/T_{eff})^{0.5} \times \exp(-5590/T_{eff})$	[32]
R41	$O_2^- + O_2(a^1\Delta_g) \rightarrow O_2(X^3\Sigma_g^-) + O_2(X^3\Sigma_g^-) + e + \varepsilon_{41}$	0.0	$k_{41} = 2.0 \times 10^{-16}$	[32]
Chemical transformations				
R42	$O(^3P) + O(^3P) + O_2(X^3\Sigma_g^-) \rightarrow O_2(X^3\Sigma_g^-) + O_2(a^1\Delta_g) + \varepsilon_{42}$	0.0	$k_{42} = 6.5 \times 10^{-45} \times (300/T_g) \times \exp(-170/T_g)$	[38]
R43	$O(^3P) + \text{wall} \rightarrow \frac{1}{2}\, O_2(X^3\Sigma_g^-)$	0.0	$\gamma_{q43} \ll 0.1$	Estimate, [39]
Diffusion				
R44	$O(^1S)$, $O(^1D)$, $O(^3P) \rightarrow$ diffusion	0.0	$D_{44} = 0.27 \times 10^{-4} \times (T_g/300)^{1.5}$	[40]
R45	$O_2(a^1\Delta_g) \rightarrow$ diffusion	0.0	$D_{45} = 0.187 \times 10^{-4} \times (T_g/300)^{1.5}$	Estimate, [41]

T_g, T_i and T_{eff} units are in K; T_e is in eV

(*) See text

relevant role in the charge transport toward the wall under the conditions considered (see [12], Fig. 3a).

Rate constants of ion–molecule reactions were determined by the effective temperature (corresponding to the kinetic energy between the ion swarm and the neutral gas in the center-of-mass frame [43]),

$$T_{eff}^{j} \equiv \frac{m_i T_g + m_j T_i}{m_i + m_j}, \tag{8}$$

where m_i and m_j are the masses of the ion and the neutral particle of the jth species, respectively, and T_i is the ion temperature depending on E/n and T_g (e.g., [44]).

The rate coefficients for almost all processes are known in the literature and are widely used for oxygen non-equilibrium discharge modelling (see, e.g. [45–50]). The rate coefficients for electron-impact excitation (R1)–(R3), dissociation (R4)–(R6), and ionization (R7) and (R11); were calculated as a function of the electron temperature by means of the solution of the electron Boltzmann equation in the classical two-term approximation using a Boltzmann solver [25] and fitted to analytic functions of T_e. The two-term approximation used seems to be reasonable under the conditions considered because this may introduce only a 20–25% error into the calculated transport and reaction coefficients for electron temperatures up to $\sim$ 40 eV [51]. The rate coefficient for the electron-impact dissociative ionization of the O_2 ($X^3\Sigma_g^-$) (reaction (R9) in Table 1) was calculated by integrating measured cross-section ($\sigma(\bar{\varepsilon})$) data [31] (which is in excellent agreement with earlier measurements [52]), over an assumed Maxwellian EEDF,

$$k_9 = \int_0^\infty \sigma(\bar{\varepsilon}) \left(\frac{8eT_e}{\pi m_e}\right)^{1/2} \frac{\bar{\varepsilon}}{T_e} \exp\left(-\frac{\bar{\varepsilon}}{T_e}\right) \frac{d\bar{\varepsilon}}{T_e}, \tag{9}$$

in the energy range T_e = 1–20 eV. Here m_e is the electron mass. Some overestimation of the rate coefficient for the reaction (R9) can occur due to the assumed Maxwellian EEDF, but only at low mean electron energy [25]. Since the higher the mean electron energy, the larger the role of the process (R9), large errors seriously affecting the model results are not expected. The calculated rate coefficient is given in Fig. 3. For comparative purposes, the corresponding rate coefficient calculated by integrating cross-section data presented in [53] over an assumed Maxwellian distribution in the range 1–7 eV [54]; is also shown in Fig. 3.

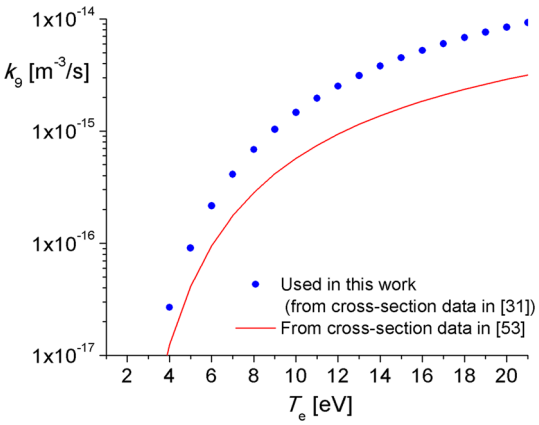

Fig. 3 Rate coefficient used for the electron-impact dissociative ionization of the ground-state oxygen molecules

However, due to the lack of measurements of the cross-sections for electron-impact dissociative ionization from the metastable oxygen molecule $O_2(a^1\Delta_g)$ (reaction (R10) in Table 1), they were assumed to be the same as for the ground state molecule but with a reduced threshold (0.98 eV) [46]. Similarly, the cross-sections for electron-impact ionization of metastable molecules (reaction (R8) in Table 1) and atoms (reactions (R12) and (R13) in Table 1) were assumed to be the same as for the corresponding ground states but with a reduced threshold.

Branching ratios for dissociative electron recombination with O_2^+ ions (reactions (R26)–(R29) in Table 1) and with O_4^+ ions (reactions (R31)–(R35) in Table 1) were taken from [34] and [32, 37], respectively. The rate of the three-body recombination for O_2^+ (reaction (R30) in Table 1) was taken from recent measurements [36], indicating a rate value larger by an order of magnitude than that reported in [32], and with a weaker dependence on T_e. The rate of three-body ion–ion recombination (reaction (R37) in Table 1) was assumed to be dependent on the negative-ion temperature T_i.

Transport Coefficients

The electron mobility and diffusivity were calculated and stored as a function of the electron temperature using a Boltzmann solver [25] in advance. The mobility of ions (often assumed to be constant [17, 23]), can significantly vary with the electric field. For high-electric field values (i.e., when the field energy is not negligible as compared with the ion thermal energy) the velocity distribution function of the ions could be very different from the distribution function of the neutral gas particles [22]. The velocity distribution is thus modeled as a Maxwellian, but the ions are assigned an ion temperature T_i, that may be much higher than T_g, the gas temperature (i.e., in the frame of the two-temperature theory [44]). Notice that a better approximation for the ion mobility in high-electric fields can be obtained in the framework of the two-temperature displaced-distribution theory [55], in which the ion distribution function, being close to the Maxwell function with a temperature that may be different from the neutral temperature, is displaced relative to the neutrals by the ion drift velocity (i.e., characterized by a non-negligible mean velocity of the ions). However, it is expected that the deviation of the high-field ion mobility be less or equal to 6% [55] for the dominant ion species (O_2^+) under the present conditions. The ion mobility in the gas mixture was calculated by the equation,

$$\frac{1}{\mu_i} \equiv \sum_j \frac{1}{\mu_j\left(T_{eff}^j\right)}, \tag{10}$$

where μ_j refers to the ion mobility in a pure gas j, but at the effective temperature of the ions for collisions with the gas j in the mixture [43].

As quoted, ions (like electrons) accelerate in electric fields and their temperature may differ significantly from the temperature of neutral species. However, the energy equation of the ions can be in general accurately solved under the 'local field approximation' (e.g. [22]). Thus, the mean translational energy of the ions in a gas mixture was described by the equation,

$$\frac{3}{2}kT_i = \frac{3}{2}kT_g + \frac{m_i + m}{2}v_{ion}^2, \quad v_{ion} = \mu_i E, \tag{11}$$

where

$$m \equiv \frac{\sum_j \omega_j m_j}{\sum_j \omega_j}, \quad \omega_j = \frac{m_j \nu_{ij}}{\left(m_i + m_j\right)^2}. \tag{12}$$

where ν_{ion} is the ion drift velocity and ν_{ij} is the momentum-transfer collision frequency of the ions with the neutral species j in the mixture [43]. The ion mobility and diffusion were related by the expression (e.g. [22]),

$$\frac{D_i}{\mu_i} = \frac{kT_i}{e}, \tag{13}$$

The required (momentum-transfer) collision integral data $\Omega_{ij}^{(1,1)}(T_{eff}^j)$ for the calculation of the ion transport coefficients were calculated using a number of methods. The collision integrals tabulated in [56] and [57] were used directly for the O_2^+–O_2 ($X^3\Sigma_g^-$) and O_2^+–$O(^3P)$ interactions, respectively. For the O_4^+–O_2 ($X^3\Sigma_g^-$) and O_4^+–$O(^3P)$ interactions, collision integral data reported in [56] and the same data as for the O_2^+–$O(^3P)$ interaction, were used; respectively. Data for the charge-exchange cross-section Q_{ex} for the O^+–$O(^3P)$ interaction, inferred from the extrapolation of the high-energy experimental data presented in [58], were used to calculate $\Omega_{ij}^{(1,1)}(T_{eff}^j)$,

$$\Omega_{ij}^{(1,1)}\left(T_{eff}^j\right) \approx 2Q_{ex}. \tag{14}$$

For the O^+–O_2 ($X^3\Sigma_g^-$) interaction, a constant value of 5.0×10^{-19} m^2 was used [59]. The mobility of the negative ion (O_2^-) was taken equal to that of the positive O_2^+ ion.

Energy transport coefficients in Eq. (4) are related to particle transport coefficients via [25],

$$\mu_\varepsilon = \frac{5}{3}\mu_e, \quad D_\varepsilon = \frac{5}{3}D_e. \tag{15}$$

In order to identify the term containing the heat conductivity, the electron energy flux term of Eq. (5) can be presented in the form [23],

$$\bar{\Gamma}_\varepsilon = \frac{5}{2}k_B T_e \bar{\Gamma}_e + q_e, \quad q_e = -\lambda_e \nabla T_e. \tag{16}$$

where $\lambda_e = \frac{5}{2}k_B n_e D_e$ [22]. Regarding to the Fourier's approximation used for the electron thermal flux q_{e}, calculations shown that the minimum characteristic length scale for gradients in the electron temperature is about one order of magnitude larger than the local electron mean-free-path, thus showing that the assumption remains reasonably well justified.

Source Terms

Volume source terms S_{k} in the particle balance Eq. (1) were determined by the reactions occurring in the discharge. This source term for the reaction jth $an_k + bn_l + \cdots \rightarrow a'n_k + cn_m + \cdots$, can be expressed using the corresponding reaction rate R_j and reaction coefficient k_j as follows,

$$S_k = \sum_j S_{kj}, \quad S_{kj} = (a - a')k_j n_k^a n_l^b \ldots = (a - a')R_j. \tag{17}$$

For example, twenty-one elementary reactions ((R7)–(R13), (R26)–(R36) and (R39)–(R41) in Table 1) contribute to the volume source term of Eq. (17) in the electron balance equation.

Nineteen elementary electron-impact reactions ((R1)–(R13) and (R30)–(R35) in Table 1) contribute to the inelastic electron energy loss term in Eq. (4). The term ΔE_j for each reaction is added in Table 1. The so-called 'recombination heating' [26, 36, 60], which can be important when the loss of electrons is dominated by three-body electron–ion recombination (reaction (R30) in Table 1) was also included in the source term $\sum_j \Delta E_j R_j$ of Eq. (4),

$$\sum_{j=26}^{36} \Delta E_j R_j = -Ik_{30} n_e^2 n_{o_2^+} + k_B n_e T_e^2 \left(\frac{d}{dT_e} \left(\sum_{j=26}^{29} k_j \right) n_{o_2^+} + \frac{dk_{30}}{dT_e} n_e n_{o_2^+} + \frac{d}{dT_e} \left(\sum_{j=31}^{35} k_j \right) n_{o_4^+} + \frac{dk_{36}}{dT_e} n_{o^+} n_{o_2} \right), \tag{18}$$

where I is the ionization energy of the O_2 ($X^3\Sigma_g^-$) (12.1 eV [22]). The last term in Eq. (18) is a correction term for energy-selective reaction rates [61] (i.e., $dk_j/dT_e < 0$ implies preferential loss of low-energy electrons, leaving the remainder with a larger mean energy), which is more important when the loss of electrons is dominated by three-body electron–ion recombination with the rate being a strong function of T_e. Heating in the process of electron detachment from negative ions and cooling in the process of electron attachment to molecules were not considered in the model.

Reactions where energy release was taken into account for the gas heating term Q_R in Eq. (6) are accompanied by the exothermic energy ε_R in the right side of the equations in Table 1. Most of the heating mechanisms considered in the present paper for an oxygen discharge were widely used in discharges in oxygen–nitrogen gas mixtures. The model considered takes into account the mechanisms of energy release suggested in [27] to describe observations at moderate values of E/n ($\sim$ 100 Td; being 1 Td $\equiv 10^{-21}$ V m^2) in air discharges, as well as the channels associated with the excitation of higher excited states of the molecules and with the formation, transformation and recombination of charged particles. These are the processes that become important at high values of E/n ($>$ 500 Td) [26]. The following processes were taken into account:

(1) Dissociation of oxygen molecules by electron-impact (reactions (R4)–(R6) in Table 1). Oxygen molecules are dissociated through the predissociation of electronic states of these molecules (e.g., [26–30]). Dissociation of O_2 ($X^3\Sigma_g^-$) into $O(^3P) + O(^3P)$, $O(^3P) + O(^1D)$, and $O(^3P) + O(^1S)$; was assumed to proceed via, respectively, the excited states $O_2(A^3\Sigma_u^+)$, $O_2(B^3\Sigma_u^-)$ and O_2^*, with energy thresholds ε_{th} of 6, 8.4 and 9.97 eV; respectively. The excitation of the higher excited state of the oxygen molecule (O_2^*) was not accounted for in [27] at moderate values of E/n, but was included in [26]. The kinetic energy of the predissociation products may be significant. In turn, 'hot' oxygen atoms are thermalized during several collisions; the energy released in these collisions is expended on the rotational excitation of molecules and gas heating. The rotational energy relaxes into the translational

degrees of freedom during 10–30 collisions (e.g., [27]). Hence, essentially all of the kinetic energy of the atoms fairly rapidly goes into gas heating. The kinetic energy of the products was calculated as,

$$\varepsilon_R = \varepsilon_{th} - \varepsilon_{diss}, \tag{19}$$

where $\varepsilon_{\text{diss}}$ is the dissociation limit of a given state. For $O_2(A^3\Sigma_u^+)$ state it was taken that $\varepsilon_4 = 0.8$ eV, for $O_2(B^3\Sigma_u^-)$ $\varepsilon_5 = 1.26$ eV; and for O_2^* it was taken that $\varepsilon_6 = 0.6$ eV [29, 30].

(2) The dissociative ionization of O_2 $(X^3\Sigma_g^-)$ (reaction (R9) in Table 1) and from the metastable state $O_2(a^1\Delta_g)$ (reaction (R10) in Table 1). It is known that, whereas electron-impact ionization of molecules AB to form AB+ produces ions with essentially the same initial kinetic energy as the AB molecule, dissociative ionization to form $A^+ + B$ results from a repulsive state of AB^+ and the products come off with significant kinetic energy [62]. The products O^+ are observed experimentally to have an average energy of $\varepsilon_9 \sim \varepsilon_{10} \sim 3$ eV [63]. These gas heating channels, that could become important at high values of E/n (> 500 Td); were not previously accounted for in high-electric field nitrogen–oxygen discharge plasma models [26, 28–30, 64, 65].

(3) Quenching of electronically excited particles (reactions (R14)–(R22) in Table 1). When the reaction products have a vibrational mode, e.g. when the reaction (R14) proceeds,

$$O_2(a^1\Delta_g) + O_2\left(X^3\Sigma_g^-\Delta\right) \rightarrow O_2\left(X^3\Sigma_g^-\Delta\right) + O_2\left(X^3\Sigma_g^-\Delta, v\right), \tag{20}$$

the excess heat of the reaction is distributed into the vibrational energy of O_2 $(X^3\Sigma_g^-,v)$ and the exothermic energy. The distribution ratio differs depending on each reaction [66, 67] and most of them were not studied. According to [27, 29, 30, 68] it was assumed that 70% of the excitation energy goes into gas heating, (while the remaining one is spent on vibrational excitation). Thus, the reactions (R14) and (R15) were considered with an energy release into gas heating of $\varepsilon_{14} = \varepsilon_{15} = 0.69$ eV, while the reaction (R16) with $\varepsilon_{16} = 1.38$ eV. The rate constant of the deactivation of $O(^1S)$ by O_2 $(X^3\Sigma_g^-)$ is $k_{17} + k_{18} = 4.3 \times 10^{-18} \times \exp(-850/T_g)$ m^3 s^{-1} [32], and according to [32, 33] the branching ratio for the production of $O(^1D)$ and $O(^3P)$ is the following:

$$\begin{aligned} O(^1S) + O_2\left(X^3\Sigma_g^-\right) \rightarrow & O(^1D) + O_2\left(X^3\Sigma_g^-, v\right) + 1.5\ \text{eV}, \quad 31\% \\ & O(^3P) + O_2(A, c, C) + 0.0\ \text{eV}. \quad 69\% \end{aligned} \tag{21}$$

Thus, the total energy converted to gas heating in reactions (R17) and (R18) is 0.48 eV (i.e., approximately 11% of the energy of the $O(^1S)$ metastable atom). It should be noted that the gas heating channels through reactions (R16) and (R17) were not accounted for in [26]. The quenching of O(1S) in reaction (R19) releases 2.20 eV into heat. The deactivation of the metastable molecules $O_2(a^1\Delta_g)$ and atoms $O(^1D)$ and $O(^1S)$ on the nozzle wall (copper) in reactions (R20)–(R22) was also taken into account through the wall loss probability γ_q. Although the deactivation of $O(^1D)$ and $O(^1S)$ on surfaces are usually very fast, the metastable $O_2(a^1\Delta_g)$ has a

relatively low destruction rate on impact with surfaces [34]. These can release a fraction of the electronic energy value into gas heating, which depends on the thermal accommodation coefficient β_T. Due to the lack of data, a value $\beta_T = 0$ was considered in the present simulation. However, in contrast to low-pressure discharges in which surface reactions can play an important role in the plasma chemistry, for high-pressures the importance of surface reactions decreases and volume reactions becomes the dominant loss mechanism for charged and excited species.

(4) Ion-conversion processes (reaction (R23)–(R25) in Table 1). It was assumed that all the energy released in the reaction (R23) and (R24) goes into heating [26]. Taking into account the binding energy (0.42 eV [37]) of the cluster O_4^+, the exothermic energy released in those reactions is $\varepsilon_{23} = 0.56$ and $\varepsilon_{24} = 0.42$ eV, respectively. Moreover, it was assumed that all the energy released in the reaction (R25),

$$O^+ + O_2\left(X^3\Sigma_g^-\Delta\right) \rightarrow O\left(^3P\right) + O_2^+(v), \tag{22}$$

goes into gas heating; including that released due to rapid relaxation of vibrational excitation of the produced $O_2^+(v)$ ions [69]. Taking into account the ionization energy of the $O(^3P)$ (13.6 eV [21]) and of O_2 ($X^3\Sigma_g^-$) (12.1 eV [22]), the exothermic energy in reaction (R25) results in $\varepsilon_{25} = 1.5$ eV.

(5) Electron–ion recombination (reactions (R26)–(R29), (R31)–(R35) and (R36) in Table 1). According to [35] the ratio between channels of the electron–ion recombination $e + O_2^+ \rightarrow$ products, is the following,

$$\begin{aligned} e + O_2^+ \rightarrow\ & O\left(^3P\right) + O\left(^3P\right) + 6.95\ \text{eV}, \quad 32\% \\ & O\left(^1D\right) + O\left(^3P\right) + 4.99\ \text{eV}, \quad 43\% \\ & O\left(^1D\right) + O\left(^1D\right) + 3.02\ \text{eV}, \quad 20\% \\ & O\left(^1D\right) + O\left(^1S\right) + 0.80\ \text{eV}. \quad 5\% \end{aligned} \tag{23}$$

Thus, the energy which goes into gas heating due to reactions (R26)–(R29) results in 5.0 eV (i.e., approximately 41% of the ionization energy of electronic ground-state oxygen molecules). Data on the products of the reaction $e + O_4^+ \rightarrow$ product are missing. In this paper, it was assumed that the recombination of the O_4^+ ion proceeds with a probability P similarly to that of the O_2^+ ion due to the relatively low value of its binding energy (0.42 eV) [37]. Thus, the energy converted to gas heating in reactions (R31)–(R34) does not exceed 4.6 eV (i.e., less than 38% of the ionization energy of the O_2 ($X^3\Sigma_g^-$) molecules). Furthermore, it was assumed that, with a probability $(1 - P)$, the channel of the reaction $e + O_4^+ \rightarrow$ product is [26, 32, 34],

$$e + O_4^+ \rightarrow O_2\left(X^3\Sigma_g^-\Delta\right) + O_2\left(X^3\Sigma_g^-\Delta\right), \tag{24}$$

and the total energy released in the reaction (R35) (which does not exceed $\varepsilon_{35} = 11.7$ eV) is converted to gas heating [26]. Moreover, it was assumed that all the ionization energy of the $O(^3P)$ (13.6 eV [22]) goes into heating in the three-body recombination reaction (R36).

(6) Ion–ion recombination (reactions (R37) and (R38) in Table 1). It was assumed that all the energy released in ion–ion recombination is spent on gas heating [26]. Taking into account the value (0.45 eV [70]) of the electron affinity with O_2 ($X^3\Sigma_g^-$), the exothermic energy released in reaction (R37) results $\varepsilon_{37} = 11.6$ eV. Taking into account also the binding energy value (0.42 eV [37]) of the O_4^+ ion, the energy converted to gas heating in reaction (R38) results in $\varepsilon_{38} = 11.2$ eV.

(7) Electron attachment and detachment (reactions (R39) and (R41) in Table 1). It was assumed that the electron affinity energy with O_2 ($X^3\Sigma_g^-$) (0.45 eV [70]) goes into gas heating in reaction (R39) (i.e., including those initially distributed over the vibrational modes of the molecule). How the released energy is shared between the products is unknown for most of the ion–molecule reactions. It was assumed that all the released energy goes to gas heating. Thus, taking into account that the energy of the $O_2(a^1\Delta_g)$ lies 0.98 eV above the electronic ground state, the exothermic energy in the detachment reaction (R41) was calculated as $\varepsilon_{41} = 0.54$ eV.

Besides, chemical transformations (reaction (R42) and (R43) in Table 1) were taken into account. It was assumed that the recombination of atomic oxygen radicals through the reaction,

$$O(^3P) + O(^3P) + O_2\left(X^3\Sigma_g^-\Delta\right) \rightarrow O_2\left(a^1\Delta_g\right) + O_2\left(X^3\Sigma_g^-\Delta, v\right), \tag{25}$$

which is exothermic by about 5 eV, produces $O_2(a^1\Delta_g)$ metastable molecules. Therefore, the exothermic energy released in reaction (R42) was taken as $\varepsilon_{42} = 2.9$ eV (i.e., 70% of the available energy) the remaining energy is spent on vibrational excitation.

In addition to the power transferred by the electrons to electronic excitation, and subsequently transferred into heat, the gas heating due to elastic collision with hot ions in the plasma–sheath boundary region was also accounted for. Due to the high mobility of the electrons the nozzle wall potential adjusts itself to be negative with respect to the surrounding plasma in the major part of its surface. As a consequence, most of the electron population is repelled in front of the wall (thus a positive space-charge sheath is formed) and the gas heating due to ion collision in high-fields could be significant. The gas heating rate term Q_{ion} in Eq. (6) was calculated as,

$$Q_{ion} = \sum_i \frac{3}{2} k_B (T_i - T_g) n_i \sum_j 2 \frac{m_{ij}}{m_i + m_j} \nu_{ij}, \tag{26}$$

where $m_{ij} \equiv m_i m_j / m_i + m_j$ is the reduced mass for the collisions between the ion of the sort i with the neutral j in the mixture. The effect of ion thermal energy becoming gas thermal energy once the ion is neutralized has not been taken into account because it amounts to a negligible correction to the energy transfer in elastic collisions between ions and neutrals, modeled by Eq. (26). The reason is that elastic cross sections between two neutral particles, and between an ion and a neutral particle, are similar, while the density of newly neutralized ions, estimated as the number of neutralizations per unit time and volume multiplied by the thermalization time, is small compared to the ion density, roughly two orders of magnitude smaller. Besides, dissociative recombination occurs mainly close to the plasma where gas and ion temperatures are similar.

Boundary Conditions

When the plasma is in contact with a material wall, charged particles hitting the wall are absorbed (or neutralized) there. The flux boundary condition for an ion of species k at the lower boundary (the nozzle wall) under the drift-diffusion approximation was taken as, (no reflection at the wall was considered) [71]

$$\bar{\Gamma}_k \cdot \hat{n} = (2a_k - 1)\mu_k \bar{E} \cdot \hat{n} n_k - \frac{1}{2}\langle v_k \rangle n_k, \tag{27}$$

where the number a_k is set to one if the drift velocity is directed toward the wall, and zero otherwise; $\hat{n}$ is an outward normal unit vector at the wall and $\langle v_k \rangle$ is the particle thermal velocity, given by,

$$\langle v_k \rangle \equiv \sqrt{\frac{8k_b T_k}{\pi m_k}}. \tag{28}$$

The ion mean-free-path for momentum transfer (defined as the ratio of the directional ion velocity to the characteristic frequency of the ion–molecule momentum exchange) is at least one order of magnitude smaller than the minimum local length scale of variation of parameters of the ion species (of the order of the Debye length); thus showing that the hydrodynamic description for the ions is well justified in the sheath, and hence there is no need for the use of Bohm criterion for the ion velocity.

The electron flux boundary condition at the nozzle wall was taken as (no reflection at the wall was considered), [71]

$$\bar{\Gamma}_e \cdot \hat{n} = -(2a_e - 1)\mu_e \bar{E} \cdot \hat{n} n_e + \frac{1}{2}\langle v_e \rangle \left(n_{\gamma,em} - n_e\right) + 2(1 - a_e)\left(-\sum_p \gamma_p \bar{\Gamma}_p\right) \cdot \hat{n}, \tag{29}$$

where $n_{\gamma,em}$ is the number density of the electrons emitted from the wall, which do not flow (back) to the wall:

$$n_{\gamma,em} \approx (1 - a_e)\frac{\sum_p \gamma_p \bar{\Gamma}_p}{\mu_e \bar{E}}, \tag{30}$$

where in the last approximation it was assumed that the electrons in front to the wall are transported by drift rather than diffusion (as is typically the case in front of negatively biased walls). According to Eq. (29) only the electrons from the bulk of the discharge contribute to the diffusive flux toward the wall. γ_p is the average number of electrons emitted per incident p ion. The ion-induced secondary electron emission, however, is not applicable in the presence of high-electric fields (as in gaps less than about 10 μm at atmospheric pressure; e.g. [72]). An explicit expression for the effective secondary electron emission coefficient γ that incorporates this ion-enhanced field emission can be obtained on the basis of the Fowler–Nordheim equation [22], as following

$$\gamma(E) = \gamma_0 + 1.56 \times 10^{-6} \frac{(\beta E)^2}{\phi} \exp\left(-\frac{6.83 \times 10^9 \phi^{1.5}}{\beta E}\right) \frac{1}{e \sum_p \Gamma_p}, \tag{31}$$

where γ_0 is the ion-induced secondary electron emission coefficient for zero electric field, ϕ is the work function (taken as 2 eV for an oxidized copper surface [22]) and β is the

geometric enhancement factor ($\sim$ 100 [15]) of the local electric field due to surface protrusions. According to [50] a value $\gamma_0 = 0.13$ was taken for both O_2^+ and O^+ ions on an oxidized metal. The same value was taken for O_4^+.

For a neutral particle of species k (including metastable particles) the flux boundary condition at the nozzle wall was taken as, [71]

$$\bar{\Gamma}_k \cdot \hat{n} = \frac{1-r}{1+r}\left(-\frac{1}{4}\langle v_k \rangle n_k - \frac{1}{2} D_k \nabla n_k \cdot \hat{n}\right), \tag{32}$$

where r is the fraction of particles reflected by the wall (= 1 for ground-state neutral particles).

The electrostatic potential at the nozzle wall was self-consistently calculated by using the total current (conduction plus displacement) conservation throughout the nozzle surface,

$$\oiint_{\text{nozzle surface}} \left(\sum_k q_k \bar{\Gamma}_k + \varepsilon_0 \frac{\partial \bar{E}}{\partial t}\right) \cdot \hat{n} dS = 0. \tag{33}$$

For the electron energy equation, the electron diffusive thermal flux $q_e = 0$ at the nozzle wall was imposed [24]. Experimental results [73] confirm that the adiabatic boundary condition for the electron energy equation is realistic. For the gas energy equation, a gas temperature of 1000 K at the nozzle wall was assumed [17].

At the sheath–plasma interface, axial profiles of plasma and gas densities as well as the electron temperature were specified as constant in time. Besides, at the upper boundary the arc voltage axial profile was specified as constant in time, corresponding in general to the conditions of the previous work [17] (i.e., the pressure distribution in the gas was assumed as a linearly decreasing function of the axial position, from 3.5 atmospheres at the nozzle inlet to 1 atmosphere at the nozzle exit; a similar axial variation was assumed for the arc voltage, varying from $-$ 80 V at the nozzle inlet, to $-$ 20 V at the nozzle exit; the electron density profile at the arc boundary was assumed as a linearly increasing function varying from 1.5×10^{18} m^{-3} at the nozzle inlet, to 1.4×10^{20} m^{-3} at the nozzle exit; the electron temperature at the arc boundary was assumed with an almost constant value of about 0.5 eV [12, 13]; besides, at the arc boundary the conservation of the particle flux was used for the O_2^-, O_4^+ and O^+ ions, whereas the density of the O_2^+ ion (the dominant ion species under the present conditions) was obtained from the quasi-neutrality of the plasma at the sheath–plasma interface). In addition, the gas diffusive thermal flux was set to zero at the sheath–plasma interface. At the nozzle inlet and exit, open boundary conditions were assumed (i.e., zero-normal derivatives of all model variables were imposed at these surfaces). Note that these conditions are only an approximation to the conditions that actually hold at the sheath–plasma interface (in fact, the location of the sheath–plasma boundary is not well defined [5]). Besides, since plasma conditions at the nozzle wall are inaccessible to plasma diagnostics if the nozzle is in a floating condition, no experimental verification was possible.

Initial Conditions

At the initial time step, a linearly interpolating function for the voltage distribution in the gas was assumed (a value of $-$ 81 V was set for the nozzle voltage). The initial distribution of the electron density obeyed the Boltzmann distribution with the electric field, while the

initial density distribution of the O_2^+ positive ion was assumed decreasing toward the nozzle due to the ions acceleration (neglecting chemical reactions). Initially, the density of other ions was assumed negligible everywhere in the gas and a uniform gas temperature (with a value of 1000 K) was assumed. The specific values used for these initial conditions did not impact on the final converged results.

Numerical Method

The fluid model equations were approximated by a finite difference discretization scheme of first-order accuracy in space and time. This method provides a higher computational speed when compared to higher-order schemes, also reducing computational and programming effort; but may introduce numerical viscosity in the solution. However, a comparison between the results obtained by solving convection–diffusion transport equations with this method, and the results obtained using a higher-order scheme; showed that, within the limits of computational errors, both results coincide [74]. The drift-diffusion fluxes in the balance equations were spatially discretized using the exponential difference scheme [75]. Due to the strong dependence of the rate coefficients and the electron diffusion coefficient on the electron mean energy, the source term in the electron energy equation was treated implicitly according to [76]. The discretized model equations were then solved iteratively by using the strongly-implicit procedure (SIP) [77]. A uniform rectangular grid with 10×20 mesh cells covered the rectangular model geometry. The mesh size in x and y directions were 0.45 mm and 0.42 μm; respectively. According to previously published results [78], the Scharfetter–Gummel scheme is accurate if the potential drop between two adjacent nodes is much less than the local electron temperature. If this condition is not satisfied, the solution obtained by this scheme exhibits excessive diffusion smoothing; thus imposing a restriction on the grid size. The distribution of the above-described condition has been obtained for the 10×20 cells grid. The results shown that the ratio of the potential drop between two adjacent nodes to the local electron temperature remains substantially lower than unity (of the order of 10^{-3} to 10^{-1}) in the whole sheath region, thus giving us confidence on the obtained numerical results. Furthermore, the accuracy of the results was checked by repeating the simulation with 10×200 mesh cells (i.e., by reducing the radial thickness of the cells by a factor of 10) with a large increase in the computational cost. The maximum relative differences in the spatial distributions of the plasma quantities in the whole computational domain were less than 17% for the electron density, 7% for the electron temperature, 5% for the electric field, 16% for the ions densities, and 20% for atomic and electronically excited species densities. Because of the stiffness of the equations (there is a wide range of time scales associated with the different processes which reduces the time step needed for accurate numerical integration) a temporal step shorter than 5×10^{-12} s was used. The equations were integrated for times of $\sim 10^{-6}$ s, which was sufficient for the density of each species to converge within an error of about 10^{-5} to its equilibrium value. It should be noted that shorter times were needed for the displacement current to be negligibly small as compared to the conduction current at the nozzle wall.

Modelling Results

The stationary number density distributions of selected gas species in the plasma–sheath boundary layer are presented in Fig. 4. As it is observed in Fig. 4a, the electron density shows a sharp drop near the plasma boundary except close to the nozzle inlet, where the field pushes the electrons deep into the sheath (as the nozzle voltage is slightly higher than that of the plasma as shown Fig. 6 (b)); with a very-low value almost everywhere inside the sheath. The non-negligible value of the electron density ($\sim 10^{16}$ m^{-3}) close to the wall at the nozzle exit is due to the ion-enhanced field emission from the wall through further ionization of $O_2(X^3\Sigma_g^-)$, mainly in reaction (R7). As at this location the (repulsive) electric field reaches a maximum (as shown Fig. 5d), this fact is expected to play a significant role in the current transfer to the wall under the double-arcing phenomenon. Figure 4b shows the distribution of the positive molecular ion density. There is a slow decrease in the O_2^+ population toward the wall, except at the nozzle inlet, where the density drops sharply due to the repulsive electric field. The composition of positive ions is dominated by O_2^+ except at the nozzle inlet, where the gas pressure is the higher. The increase in gas pressure results in an increase in the O_4^+ density (not showed) associated to a decrease in the O_2^+ density through the fast three-body ion-conversion in reaction (R24). A relatively high negative ion density is observed close to the nozzle inlet (as shown Fig. 4c) due to electron attachment in reaction (R39). However, as the electron density distribution results comparable with that of O_2^- inside the layer, the negative ion current toward the wall resulted negligible as compared with the electron one, consistent with previous experiments (see [12], Fig. 3a).

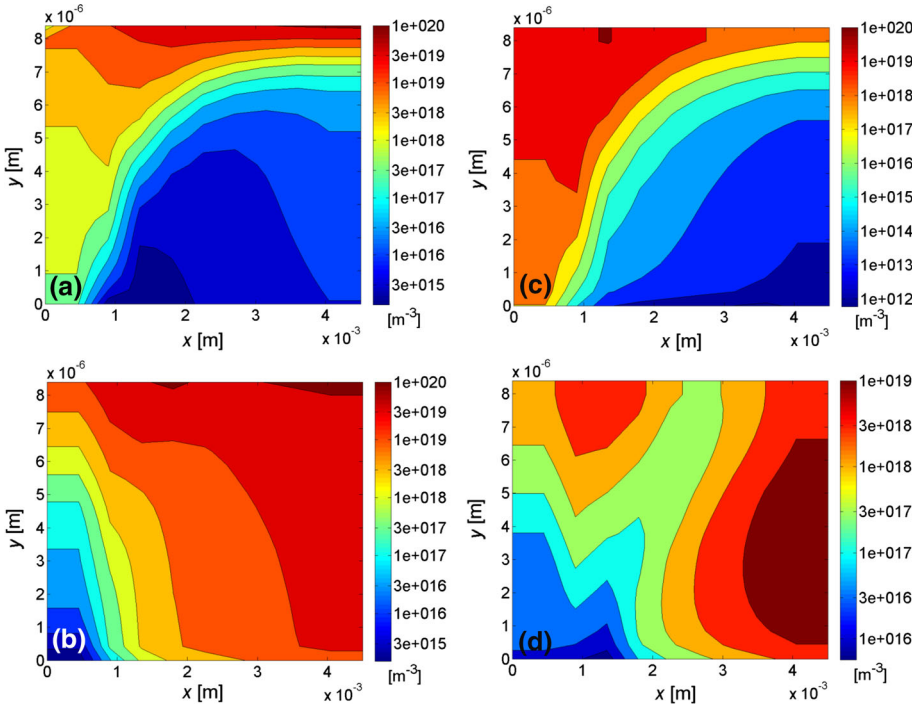

Fig. 4 2D number density profiles of electrons (**a**), O_2^+ (**b**), O_2^- (**c**) and $O(^1D)$ (**d**)

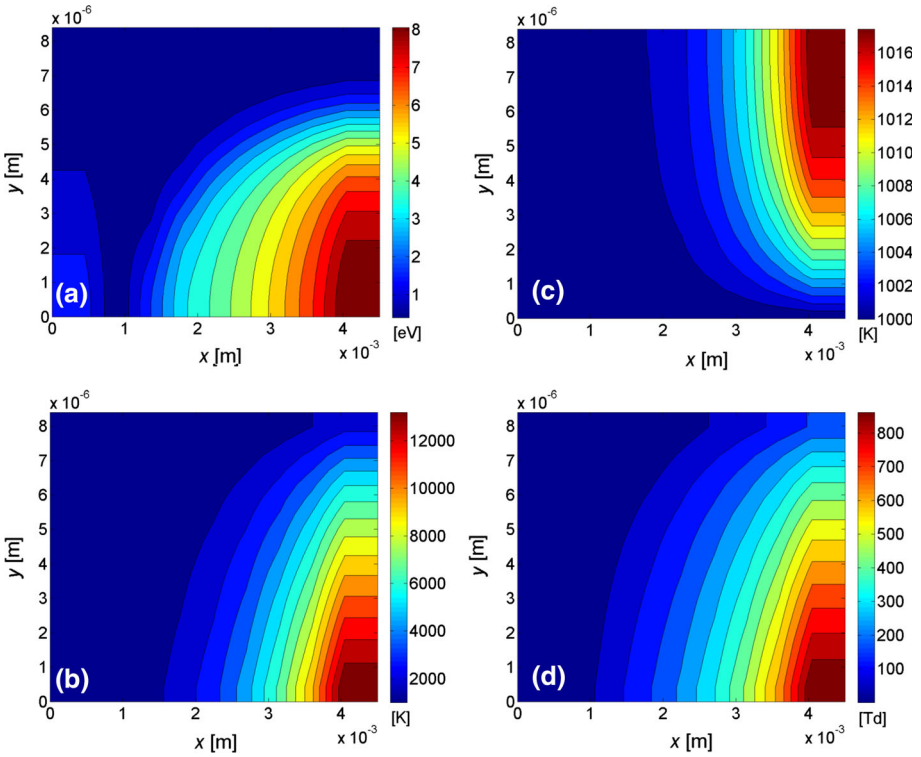

Fig. 5 2D temperature profiles of electrons (**a**), O_2^+ (**b**), gas (**c**); and 2D profile of E/n (**d**)

Figure 4d shows the spatial profile of the metastable $O(^1D)$. The distribution of the $O(^1D)$ is mainly constituted of the contributions from both dissociation of $O_2(X^3\Sigma_g^-)$ into $O(^3P) + O(^1D)$ in reaction (R5), as well as dissociative recombination of O_4^+ and O_2^+ ions in reactions (R32)–(R34), and (R27)–(R29); respectively. This is manifested by an increase in the $O(^1D)$ density at the nozzle exit where the electron-impact excitation processes are important (as shown Fig. 7b) and also by an additional peak close to the plasma boundary where the dissociative recombination predominates (as shown Fig. 7c).

The stationary temperature distributions of electrons, O_2^+ ions and neutral particles (gas), together with the reduced electric field, are given in Fig. 5. As it is observed in Fig. 5a, the electron temperature varies from about 0.5 eV at the plasma boundary to quite high-values ($\sim$ 8–9 eV) at the wall close to the nozzle exit, where the local values of the electric field are very high ($\sim$ 900 Td, as shown Fig. 5d). According to a numerical solution of the Boltzmann equation for electrons, the (local field) equilibrium value of the electron temperature is $\sim$ 18 eV for $E/n = 900$ Td, considerably higher than that found by solving the electron energy equation; thus, suggesting that under the conditions considered the local field approximation does not hold for electrons. The O_2^+ ions temperature is shown in Fig. 5 (b). Expectedly, their temperature ($\sim$ 12,000 K) is well decoupled from the temperature of neutral species (shown in Fig. 5c) where high-electric field occur. However, the ion component of the gas is thermally isolated from the nozzle wall (as the gradient of the ion temperature vanishes there) and does not pose a potential danger to the nozzle wall surface. Besides, as is it observed in Fig. 5c, the gas temperature remains

everywhere close to the temperature of the nozzle surface (due to the heat transfer to the wall), with minor departures ($\sim$ 2%) at the nozzle exit. This increase in the gas temperature is not caused by the fast transfer of electron energy into thermal energy through the mechanism proposed in the term Q_R in Eq. (6); but by the energy released into heat through elastic collisions between hot ions and neutrals particles (as is shown in Fig. 8d). However, it is expected that the fast gas heating plays a significant role in the development of the double-arcing instability [13]. From Fig. 5d it is observed that the reduced electric field considerably varies in the sheath–plasma boundary region, from low values ($\sim$ 10 Td) near to the plasma boundary to high values ($\sim$ 900 Td) at the nozzle wall.

The current density axial distributions for electrons and positive ions at the nozzle wall are presented in Fig. 6a. The potential drop accelerates the positive ion population toward the nozzle wall and repels a considerable number of the electrons to maintain the zero-current balance. It is observed that the electron current is concentrated mostly at the nozzle inlet, where the radial electric field is directed toward the plasma (as shown Fig. 6b), thus reaching a relatively high current density value of $\sim$ 4 A/cm^2; whereas the positive ion current (mainly transported by O_2^+ ions) is dominant in the bulk of the sheath. Notice that the ion current is collected by almost the entire nozzle inner surface in a diffuse fashion, with a lower current density ($\leq$ 1 A/cm^2). This numerical result confirms that the zero-current balance in the nozzle is fulfilled globally along the whole collecting area of the

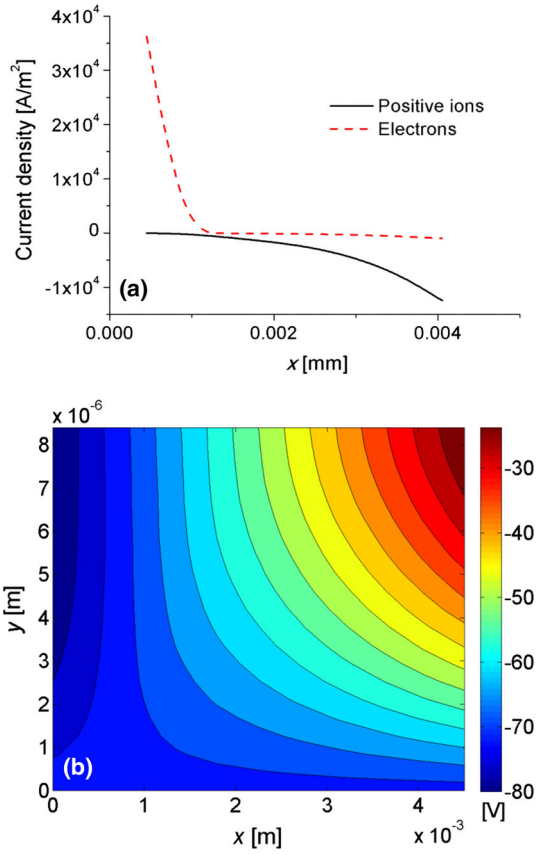

Fig. 6 Electron and positive ion current densities at the nozzle wall (**a**); and 2D profile of the gas voltage (**b**)

nozzle (and not locally); giving rise to a non-equilibrium unipolar discharge of weak current (of about 0.05 A) through the nozzle. A very low-electron emission from the nozzle wall into the plasma, due to ion-enhanced field emission can be also seen toward the nozzle exit. From Fig. 6b it is observed that the voltage drop between the metallic nozzle and the plasma at the nozzle exit reaches a value very close to the total arc voltage drop inside the nozzle, giving rise there to a local electric field of high magnitude (around 900 Td according to Fig. 5d). The voltage of the floating nozzle resulted around − 71 V, in agreement with measurements (− 75 ± 6 V) [12]. Besides, it is seen in Fig. 6b that the linearly varying potential of the quasi-neutral plasma along the axial direction is smoothly joined at the interface by the potential in the sheath, with the radial electric field at this interface (as shown Fig. 5d) being of the order of the local ambipolar value [e.g., 79]. Note that no quasi-neutrality is imposed inside the sheath, so that any marked deviation from this state near the plasma–sheath interface would show in the form of a large radial component of the electric field at this boundary, thus no merging correctly into the ambipolar field at the plasma side.

The profiles of some electron-impact reaction rates are shown in Fig. 7. As it is observed in Fig. 7a, the total ionization rate (through reactions (R7)–(R13)) reaches a maximum at a location close (but not identical) to the maximum of the mean-energy of the electrons (as shown Fig. 5a). The main channel of production of O^+ ions is through the dissociative ionization of $O_2(X^3\Sigma_g^-)$ molecules in reaction (R9). However, under the conditions considered, the concentration of the O^+ ions is negligible small as compared to that of the $O_2{}^+$ ions. Expectedly, the electron-impact dissociation in reactions (R4)–(R6) occurs at the same location to that of the ionization (as shown Fig. 7b). Besides, the dissociative electron recombination rate in reactions (R26)–(R29) is presented in Fig. 7c. It is observed that the depletion of the positive ion density in the sheath region due to the ion flux to the nozzle wall affects the ionization balance (i.e., the ionization prevails over the recombination toward the nozzle wall). Ions born in the sheath region diffuse to the nozzle wall where they recombine. However, the lack of electrons at the nozzle exit hampers the double-arcing development.

The profiles of the Joule heating of electrons and of the electron energy loss in inelastic collisions are presented in Fig. 8a, b, respectively. The electron heating profile shows a large positive peak value ($\sim 10^{10}$ W/m^3) in the vicinity of the nozzle inlet region (where the electron flux is the largest, as shown Fig. 6a), with relatively low heating in the bulk of the sheath region. Moreover, a slight negative heating (electron cooling) is also observed in a relative large region of the bulk of the sheath. Notice that the electrons lose energy when diffusing against the field, reducing their mean-energy and therefore reducing the magnitude of the diffusivity. This occurs where the electric field is relatively low ($\leq$ 100 Td). As discussed in [80], the local field approximation fails to account for this, mistakenly assigning a too-large value of electron diffusivity. From Fig. 8b it is seen that the electron energy loss through inelastic collision reaches a peak near the nozzle exit, where dissociation and ionization occur. Notice the strong nonlocal energy deposition regime of the electrons. The electron heating in the three-body recombination reaction (R30) is presented in Fig. 8c. As it is observed, the recombination heating profile shows a relatively large peak value ($\sim 10^9$ W/m^3) in the vicinity of the plasma boundary where the electron recombination prevails. In addition, Fig. 8d shows the profile of the Joule heating of positive ions (i.e., the gas heating rate through elastic collisions with hot ions under the local field approximation). It is observed that the positive ion heating profile presents a large peak value ($\sim 10^{10}$–10^{11} W/m^3) in the vicinity of the nozzle exit (where the positive

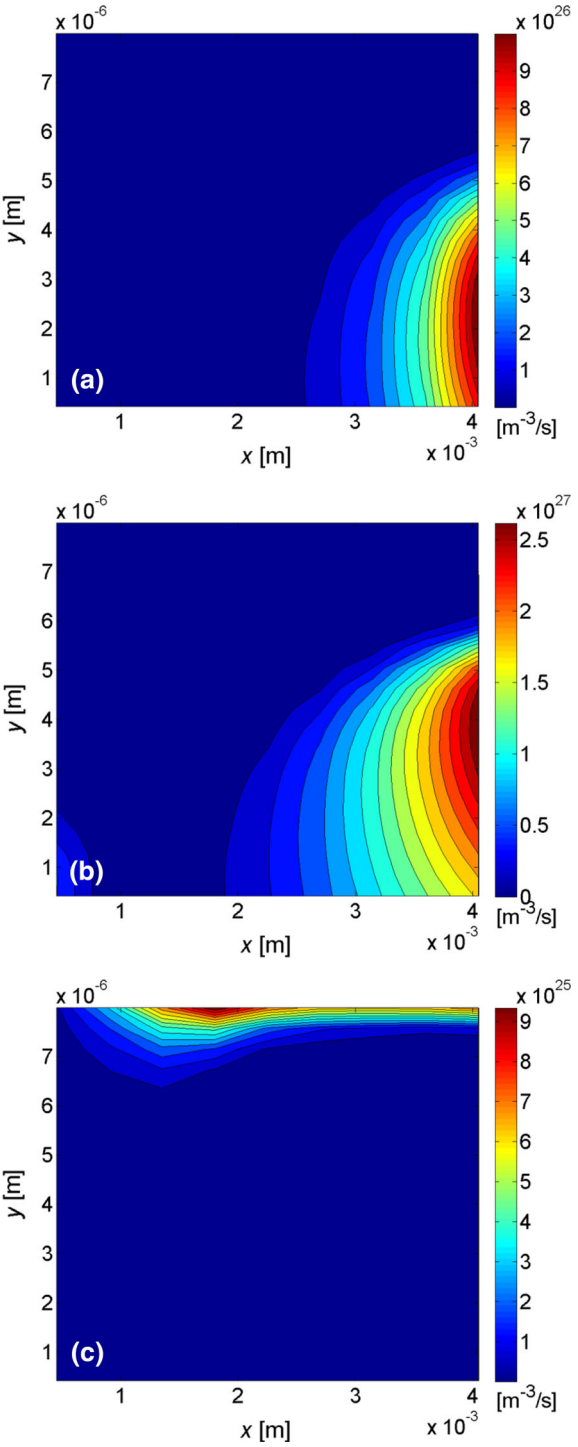

Fig. 7 2D profiles of the total ionization rate (**a**), dissociation rate (**b**) and electron–ion recombination rate (**c**)

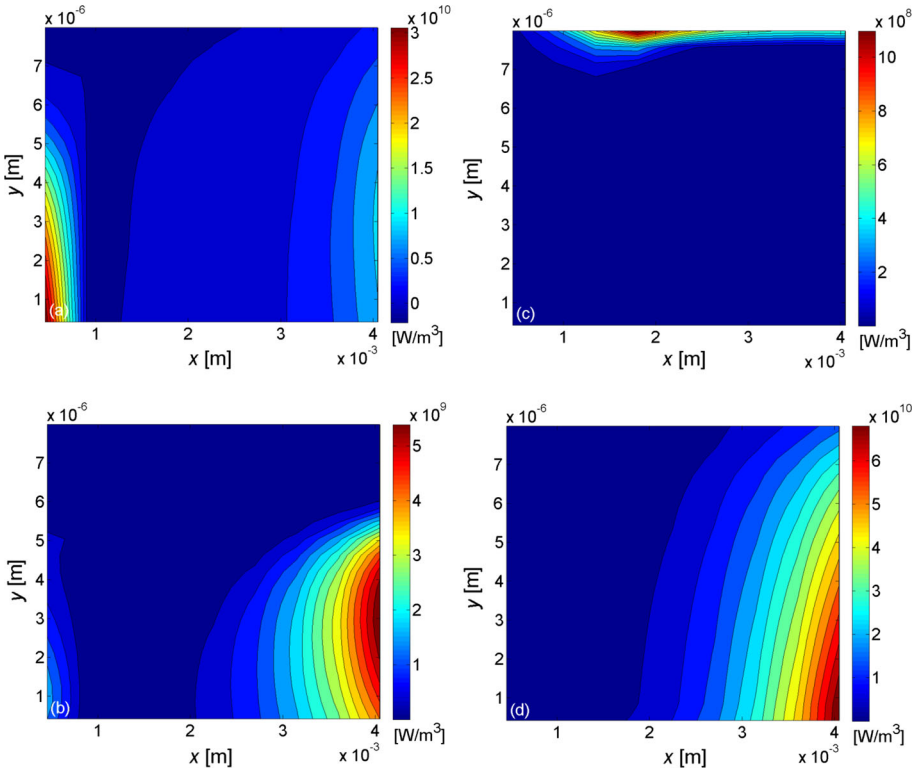

Fig. 8 2D profiles of the Joule heating (or cooling) of electrons (**a**), electron energy loss in inelastic collisions (**b**), electron–ion recombination heating (**c**) and Joule heating of ions (**d**)

ion flux is the largest, as shown Fig. 6a), with relatively low heating in the bulk of the sheath region.

The amount of the total power delivered in the bulk of the sheath region under the conditions considered is $\sim$ 1700 mW. A large part ($\sim$ 80%) of the total power is spent on heating the positive ions (which is further dissipated through collisions with the neutral particles). This arises because of the zero-current balance at the nozzle wall (most of the electron population is repelled in front of the nozzle wall as the nozzle potential is negatively biased with respect to the surrounding plasma in the major part of its surface). The remainder part of the total power is spent on heating the electrons. The electron power is partially consumed in the production of electronically excited particles and in the dissociation and ionization processes through reactions (R1)–(R13) and (R30)–(R35). The electron energy loss in the bulk of the sheath was calculated as follows,

$$\varepsilon_{loss} = \sum_j \left(\Delta E_j \int_V R_j dV \right), \tag{34}$$

where V is the calculation volume. $\varepsilon_{\text{loss}}$ represents only about 25% of the electron power, the rest is transported by the electron enthalpy flux and heat conduction. This result also supports the strong nonlocal energy deposition regime of the electrons. Figure 9 shows the fraction of the total electron energy loss attributed to selected reactions in Table 1. Over

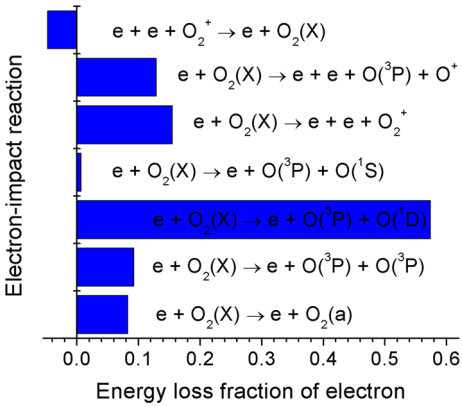

Fig. 9 Energy loss fractions of electrons by the electron-impact collision processes listed in Table 1

57% of the electron power is consumed by the dissociation of O_2 ($X^3\Sigma_g^-$) into $O(^3P) + O(^1D)$ in reaction (R5), the other dissociation channels ($O(^3P) + O(^3P)$ and $O(^3P) + O(^1S)$), consume 9 and 0.7%, respectively. The rest of the electron power is used in ionization processes of $O_2(X^3\Sigma_g^-)$ ($\sim$ 29%) and in the production of the molecular metastable $O_2(a^1\Delta_g)$ in reaction (R1) ($\sim$ 8%). Notice that the contribution of the recombination heating in reaction (R30) is not negligible, accounting for $\sim$ 4% of the total electron power.

The profile of the gas heating rate in chemical reactions is shown in Fig. 10, while the main contributions are presented in Fig. 11. About 63% of the power spent on gas heating is produced by the ion–molecule reaction (R24), the electron–ion and ion–ion (through $O_2^+ + O_2^- + O_2(X^3\Sigma_g^-)$ and $O_4^+ + O_2^-$ → products) recombination reactions (R31)–(R34) and (R37) and (R38); respectively, and by the attachment reaction (R39). The rest of the power converted into heat is contributed by dissociation in reaction (R4)–(R6), dissociative ionization in reaction (R9) and quenching of $O(^1D)$ metastable in reaction (R16). This is indicated by a peak ($\sim$ 10^9–10^{10} W/m^3) in the gas heating rate at the vicinities of the plasma boundary, where the electron–ion and ion–ion recombination and also the attachment are important; and also by an additional (and lower) peak at the same location where the high-threshold electron-impact reactions occur. It is expected that this additional peak in the gas heating rate (through reactions (R4)–(R6), (R9) and (R16)) plays a key role in the triggering of the double-arcing phenomenon [13]. During the calculations, it was assumed that the dissociation of the oxygen molecules is of high probability ($P = 1$) in the electron–ion reaction $e + O_4^+$ → product, (R31)–(R34); according to [28]. Thus, the energy converted into heat in this reaction results 4.6 eV (instead of 11.7 eV if the dissociation of the oxygen molecules is taken to be of low-probability). As over 10% of the power spent on gas heating is produced by this reaction (as shown Fig. 11), such an assumption has a non-negligible effect on the contribution of the exothermic processes to the overall balance of the gas heating in the discharge.

As discussed in [28], ion–molecule reactions, electron–ion reactions and ion–ion recombination are major processes for heating gas in air discharges at $E/n > 400$ Td. However, under the conditions considered, such high electric field occurs only at the vicinities of the wall surface close to the nozzle inlet (as shown Fig. 5d), but where the ionization prevails over the recombination (as the ion flux to the nozzle wall affects the ionization balance). Notice that the studied discharge is not a quasi-neutral plasma, so the results regarding the dependence on E/n of the contribution of the exothermic processes to

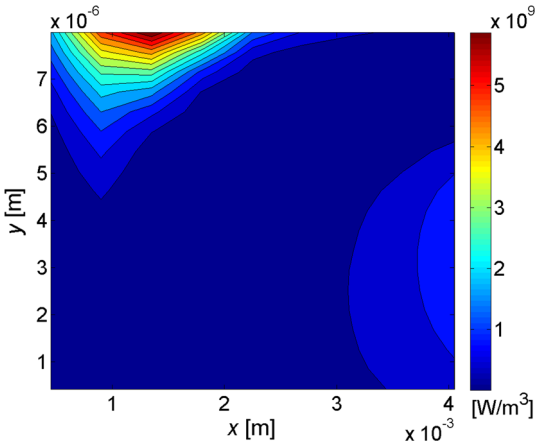

Fig. 10 2D profile of the fast gas heating rate in chemical reactions

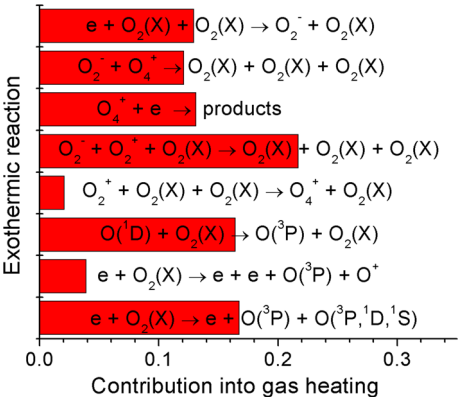

Fig. 11 Distribution of energy release in fast gas heating for the different processes considered

the overall balance of the gas could be different to those found in discharge plasmas [26–30, 64, 65, 68].

Conclusions

A numerical investigation of the properties of the non-equilibrium unipolar discharge in the plasma–sheath boundary region of a cutting arc torch operated with oxygen was presented. The nonlocal transport of electrons into the fluid model was accounted for. A detailed mechanism of fast gas heating was discussed. The following conclusions were drawn from this study:

1. The electron temperature varies from about 0.5 eV at the plasma boundary to quite high-values ($\sim$ 8–9 eV) deep in the sheath where the local values of the electric field are very high ($\sim$ 900 Td). The ion temperatures ($\sim$ 10,000 K) are well decoupled from the gas temperature ($\sim$ 1000 K) where high-electric field arises.
2. The electron current is concentrated mostly at the nozzle inlet where the radial electric field is directed toward the plasma, thus reaching a relatively high current density

value of $\sim$ 4 A/cm^2, whereas the positive ion current (mainly transported by O_2^+ ions) is dominant in the bulk of the sheath; giving rise to a non-equilibrium unipolar discharge of weak current (of about 0.05 A) through the nozzle.

3. The amount of the total power delivered in the bulk of the sheath region under the conditions considered is $\sim$ 1700 mW. A large part ($\sim$ 80%) of the total power is spent on heating the positive ions (which is further dissipated through collisions with the neutral particles).
4. The electron energy loss in inelastic collisions represents only $\sim$ 25% of the electron power; the rest is transported by the electron enthalpy flux and heat conduction. Over 57% of the electron power is consumed by the dissociation of O_2 ($X^3\Sigma_g^-$) into $O(^3P) + O(^1D)$, the other dissociation channels consume $\sim$ 10%. The rest of the electron power is used in ionization processes of $O_2(X^3\Sigma_g^-)$ ($\sim$ 29%) and in the production of the molecular metastable $O_2(a^1\Delta_g)$ by electron-impact excitation ($\sim$ 8%). The contribution of the recombination heating is not negligible, accounting for $\sim$ 4% of the total electron power.
5. About 63% of the power spent on gas heating is produced by the ion–molecule reaction, the electron–ion and ion–ion (through $O_2^+ + O_2^- + O_2(X^3\Sigma_g^-)$ and $O_4^+ + O_2^- \rightarrow$ products) recombination reactions, and by the electron attachment. The rest of the power converted into heat is contributed by dissociation by electron-impact, dissociative ionization and quenching of $O(^1D)$. It is expected that the later reactions play a key role in the triggering of the double-arcing phenomena in oxygen gas.

Acknowledgements This work was supported by Grants from the CONICET (PIP 11220120100453) and Universidad Tecnológica Nacional (PID 2264 and 4626). L. P. and F. O. M. are members of the CONICET. J. C. C. thanks the CONICET for his doctoral fellowship.

References

1. Riemann KU (1991) J Phys D Appl Phys 24:493–518
2. Riemann KU (2003) J Phys D Appl Phys 36:2811–2820
3. Franklin RN (2003) J Phys D Appl Phys 36:R309–R320
4. Franklin RN (2003) J Phys D Appl Phys 36:2821–2824
5. Franklin RN (2004) J Phys D Appl Phys 37:1342–1345
6. Benilov MS (2009) Plasma Sources Sci Technol 18:014005
7. Brinkmann RP (2011) J Phys D Appl Phys 44:042002
8. Hill RJ, Jones GR (1979) J Phys D Appl Phys 12:1707–1720
9. George DW, Richards PH (1968) Brit J Appl Phys 1:1171–1182
10. Nemchinsky VA, Severance WS (2006) J Phys D Appl Phys 39:R423–R438
11. Boulos M, Fauchais P, Pfender E (1994) Thermal plasmas, fundamentals and applications, vol 1. Plenum Press, New York
12. Prevosto L, Kelly H, Mancinelli B (2009) J Appl Phys 105:013309
13. Prevosto L, Kelly H, Mancinelli B (2011) J Appl Phys 110:083302
14. Gielen HJG, Schram DC (1990) IEEE Trans Plasma Sci 18:127–133
15. Insepov Z, Norem J (2013) J Vac Sci Technol, A 31:011302
16. Nemchinsky VA (2009) J Phys D Appl Phys 42:205209
17. Mancinelli B, Minotti FO, Prevosto L, Kelly H (2014) J Appl Phys 116:023301
18. Prevosto L, Kelly H, Mancinelli B (2009) J Appl Phys 105:123303
19. Prevosto L, Mancinelli B, Kelly H (2008) Phys Scr T131:014026
20. Boeuf JP, Pitchford LC (1995) Phys Rev E 51:1376–1390
21. Sheridan TE, Goree J (1991) Phys Fluids B 10:2796–2804
22. Raizer YP (1991) Gas discharge physics. Springer, Berlin

23. Rafatov I, Bogdanov EA, Kudryavtsev AA (2012) Phys Plasmas 19:033502
24. Chen G, Raja LL (2004) J Appl Phys 96:6073–6081
25. Hagelaar GJM, Pitchford LC (2005) Plasma Sources Sci Technol 14:722–733
26. Aleksandrov NL, Kindysheva SV, Nudnova MM, Starikovskiy AY (2010) J Phys D Appl Phys 43:255201
27. Popov NA (2001) Plasma Phys Rep 27:886–896
28. Popov NA (2011) J Phys D Appl Phys 44:285201
29. Mintoussov EI, Pendleton SJ, Gerbault FG, Popov NA, Starikovskaia SM (2011) J Phys D Appl Phys 44:285202
30. Pintassilgo CD, Guerra V (2015) Plasma Sources Sci Technol 24:055009
31. Krishnakumar E, Srivastava SK (1992) Int J Mass Spectrom Ion Proc 113:1–12
32. Kossyi IA, Kostinsky AY, Matveyev AA, Silakov VP (1992) Plasma Sources Sci Technol 1:207–220
33. Slanger TG, Black G (1978) J Chem Phys 68:998–1000
34. Capitelli M, Ferreira CM, Gordiets BF, Osipov AI (2000) Plasma kinetics in atmospheric gases. Springer, New York
35. Florescu-Mitchell AI, Mitchell JBA (2006) Phys Rep 430:277–374
36. Aleksandrov NL, Anokhin EM, Kindysheva SV, Kirpichnikov AA, Kosarev IN, Nudnova MM, Starikovskaia SM, Starikovskii AY (2012) J Phys D Appl Phys 45:255202
37. Dulaney JL, Biondi MA, Johnsen R (1998) Phys Rev A 37:2539–2542
38. Johnston HS (1968) Technical Report NSRDS-NBS-20, National Bureau of Standards
39. Gomez S, Steen PG, Grahama WG (2002) Appl Phys Lett 81:19–21
40. Yolles RS, Wise H (1968) J Chem Phys 48:5109–5113
41. Weissman S, Mason EA (1962) J Chem Phys 37:1289–1300
42. Turner MM (2015) Plasma Sources Sci Technol 24:035027
43. Viehland LA, Mason EA (1995) At Data Nucl Data Tables 60:37–95
44. Mason EA, McDaniel EW (1988) Transport properties of ions in gases. Wiley, New York
45. Gudmundsson JT, Marakhtanov AM, Patel KK, Gopinath VP, Lieberman MA (2000) J Phys D Appl Phys 33:1323–1331
46. Gudmundsson JT, Kouznetsov IG, Patel KK, Lieberman MA (2001) J Phys D Appl Phys 34:1100–1109
47. Gudmundsson JT (2004) J Phys D Appl Phys 37:2073–2081
48. Vagin NP, Ionin AA, KlimachevYuM Kochetov IV, Napartovich AP, Sinitsyn DV, Yuryshev NN (2003) Plasma Phys Rep 29:211–219
49. Toneli DA, Pessoa RS, Roberto M, Gudmundsson JT (2015) J Phys D Appl Phys 48:325202
50. Hannesdottir H, Gudmundsson JT (2016) Plasma Sources Sci Technol 25:055002
51. Phelps AB, Pitchford LC (1985) Phys Rev A 31:2932–2949
52. Rapp D, Briglia D (1965) J Chem Phys 43:1480–1489
53. Eliasson B, Kogelschatz U (1986), Rep. No. CH-5405 (Brown BoveriForschungszentrum, Baden)
54. Lieberman MA, Lichtenberg AJ (1994) Principles of plasma discharges and materials processing. Willey, New York
55. Almeida PGC, Benilov MS, Naidis GV (2002) J Phys D Appl Phys 35:1577–1584
56. Ellis HW, Pai RY, McDaniel EW, Mason EA, Viehland LA (1976) At Data Nucl Data Tables 17:177–210
57. Levin E, Wright MJ (2004) J. Thermophys Heat Transf 18:143–147
58. Lindsay BG, SieglaffDR Smith KA, Stebbings RF (2001) J Geophys Res 106:8197–8203
59. Lee C, Graves DB, Lieberman MA, Hess DW (1994) J Electrochem Soc 41:1546–1555
60. Ardelyan NV, Bychkov VL, Kochetov IG, Kosmachevskii KV (2011) IEEE Trans Plasma Sci 39:3326–3330
61. Robson RE (1986) J Chem Phys 85:4486–4501
62. Rapp D, Englander-Golden P, Briglia DD (1965) J Chem Phys 42:4081–4085
63. Capitelli M, Bardsley JN (1989) Non–equilibrium processes in partially ionized gases. Plenum Press, New York
64. Popov NA (2016) Plasma Sources Sci Technol 25:044003
65. Flitti A, Pancheshnyi S (2009) Eur Phys J Appl Phys 45:21001
66. Piper LG (1988) J Chem Phys 88:231–239
67. Piper LG (1988) J Chem Phys 88:6911–6921
68. Komuro A, Ono R (2014) J Phys D Appl Phys 47:155202 (13 pp)
69. Ferguson EE (1986) J Phys Chem 90:731–738
70. Ervin KM, Anusiewicz I, Skurski P, Simons J, Lineberger WC (2003) J Phys Chem A 107:8521–8529
71. Hagelaar GJM, de Hoog FJ, Kroesen GMW (2000) Phys Rev E 62:1452–1454
72. Go DB, Pohlman DA (2010) J Appl Phys 107:103303

73. Leveroni E, Pfender E (1989) Rev Sci Instrum 60:3744–3749
74. Pancheshnyi SV, Starikovskii AY (2003) J Phys D Appl Phys 36:2683–2691
75. Scharfetter DL, Gummel HK (1969) IEEE Trans Electron Devices 16:64–77
76. Hagelaar GJM, Kroesen GMW (2000) J Comp Phys 159:1–12
77. Stone HL (1968) SIAM J Numer Anal 5:530–558
78. Kulikovsky AA (1995) J Comp Phys 119:149–155
79. Godyak A, Sternberg N (1990) Phys Rev A 42:2299–2312
80. Sakiyama Y, Graves DB (2007) J Appl Phys 101:073306